Journal of the Australian Ceramic Society (2022) 58:683–697
https://doi.org/10.1007/s41779-022-00720-7

RESEARCH

Structural, electronic and electrical conduction behaviour of Gd^{3+} doped $Ca_{2-x}Y_2O_5$ metal oxide ceramic synthesised by solid state reaction method

Sadhana Agrawal[1]

Received: 30 October 2021 / Revised: 28 January 2022 / Accepted: 13 February 2022 / Published online: 6 March 2022

Abstract

The present paper reports the structural, electronic and electrical conduction mechanisms of $Ca_{2-x}Y_2O_5$:xGd^{3+} ($x = 0$, 0.03 and 0.05 mol%) metal oxides synthesised by solid state reaction method. The computational crystal structure analysis confirms the formation of cubic structure along with space group Ia-3. The structural analysis confirms the shifting of the most intense peak towards the higher Bragg angle side. The morphological analysis shows the formation of clusters of grain of irregular shape and size. The frequency-dependent dielectric studies show that orientational and space charge polarisation are the dominant mechanisms in prepared compounds. The complex impedance spectroscopy shows that the conduction mechanism in $Ca_{2-x}Y_2O_5$:Gd^{3+} metal oxide is due to grain and grain boundary effect. The electrical modulus spectroscopy reveals the hopping of charge carriers between Ca^{2+} site and O^{2-} site, respectively. The electrical conductivity in prepared metal oxide is due to small polaron hopping mechanism.

Keywords Ceramic · DFT · X-ray diffraction · Complex impedance spectroscopy · AC conductivity

Introduction

Metal oxides are the crystalline solids which can be modified into different structural geometries with metallic, semiconducting or insulating behaviour [1]. The general formula of metal oxide is (MO) where M can be substituted by metal cations like Ca^{2+}, Y^{3+}, La^{3+} etc. and O is an oxide anion [2]. The alkali and alkaline earth metal reacts with oxygen atom to form different oxidation states [3]. On the basis of different oxidation states and bond nature, metal oxide compounds are categorised as (1) oxides (O^{2-}), (2) peroxides ($O_2{}^{2-}$) and (3) superoxides (O^{2-}) [4]. Peroxide compounds contain oxygen–oxygen covalent single bonds whereas super oxides contain oxygen–oxygen covalent bonds [5]. Metal oxides show unique physical and chemical properties due to their morphology and high densified grains [6]. It can be used as in various technological industries such as in the fabrication of sensors, fuel cells, circuits, catalysts and coatings against corrosion [7].

Metal oxides have drawn the attention of researchers in the field of dielectric, optical and electronic studies for a wide range of applications such as sensors, capacitors, data storage devices, and optical and display devices. Som et al. reported about the lanthanum co-doped Y_2O_3, which shows the formation of cubic structure [8]. Qian et al. reported about the Eu^{3+} doped Yb_2O_3 and confirms the formation of cubic phase [9]. Srinivasen et al. reported that the dielectric properties in NiO/CuO/ZnO combined semiconductor metal oxide are due to Maxwell–Wagner polarisation [10]. Ambalagi et al. reported about the structural and dielectric properties of NiO synthesised by solution combustion method. The reported XRD analysis reveals the formation of cubic structure. In the dielectric studies, the dielectric constant and loss decreases with increase in frequency, whereas the value of AC conductivity increases with the increase in frequency and weight percentage [11]. Saxena et al. reported about the structural and dielectric properties of Cr doped $Mg_{0.5}Zn_{0.5-x}CO_2O_4$ metal oxide synthesised by solid state reaction. The study reports the formation of cubic structure with space group Fm3m. The dielectric constant and loss decrease with the increase in frequency and become

---

✉ Sadhana Agrawal
sagrawal.phy@nitrr.ac.in

[1] Department of Physics, National Institute of Technology, Raipur 492010, India

constant at higher frequencies, which shows that interfacial polarisation is the dominant mechanism [12]. Lakhane et al. reported about dielectric properties of zeolite-based metal oxide nanocomposites, which shows that the AC conductivity remains constant in low-frequency region which increases linearly in the high-frequency region [13]. Tack et al. reported about the structural and electronic properties of transition metal oxide attached to a single-walled carbon nanotube. Structural analysis reveals the formation of a cubic structure and electronic structure that show a band gap value of 1.33 eV [14]. Skorodumova et al. reported about the electronic properties of alkaline-earth metal oxides. The reported result reveals that the metal oxide has a cubic structure with a band gap value of 4.4 eV [15]

Some of the metal oxides such as TiO_2, ZrO_2 and HFO_2 show high value of dielectric constant and electrical permittivity [16]. Dielectric constant is the relative permittivity which is defined as the measure of electronic polarisability of a material which varies with temperature, frequency, humidity etc. [17]. Metal oxides are the narrow band gap materials with a large leakage current [18]. By the addition of rare earth dopants, the thermal stability and leakage current of metal oxides have been improved [19]. However, due to addition of rare earth dopants, the dielectric constant of some metal oxides decreases due to low dielectric constant value of rare earth dopants [20].

Solid state reaction or ceramic route is a self-diffusion technique that provides cost-effective, environmentally friendly conditions for the mixing of solids at high temperatures ranging from 1000 to 1500 °C [21, 22]. The factors that affect the solid-state reaction technique is reaction time, melting point of solids, reaction rate, free energy, surface area of solids etc. [23].

This paper reports the electrical conduction and dielectric behaviour of gadolinium doped calcium yttrium oxide synthesised by solid-state reaction method. The structural and morphological analyses were done to confirm the phase and crystal structure of prepared compound. Frequency-dependent dielectric studies show the dominant polarisation effect in the compound. The complex impedance spectroscopy and electrical modulus spectroscopy confirm the transport of charge carrier and relaxation behaviour of compounds. Frequency-dependent AC conductivity shows the nature of the material suitable for fabrication of microelectronic devices.

Methods

Synthesis of $Ca_{2-x}Y_2O_5$:xGd^{3+} ceramic.

The samples were synthesised by using solid state reaction method. All the starting materials, i.e. CaO (99.99%), Y_2O_3 (99.99%), Gd_2O_3 (99.99%) with particle size of CaO (500 nm), Y_2O_3 (< 100 nm) and Gd_2O_3 (5.9 ± 0.13 nm), were manufactured by Sigma Aldrich. All the starting materials were taken in stoichiometric ratios. First, 0.27 mol of CaO and 0.27 mol of Y_2O_3 were mixed with Gd_2O_3 with molar concentration of Gd_2O_3 varying from 0 to 0.05 mol%. The materials were then ground in agate mortar and pestle for 1 h by using acetone as a solvent. The powdered samples were then kept in a programming furnace at 1200 °C for calcination. The calcined powder was again ground for 45 min and kept in furnace at 1100 °C for sintering. The synthesised powder was then converted into pellets and silver paste was brushed on both sides of the pellets acting as cathode and anode. The pellets were then dried in an oven at 100 °C for 1 h. Figure 1 shows the flowchart of synthesis route.

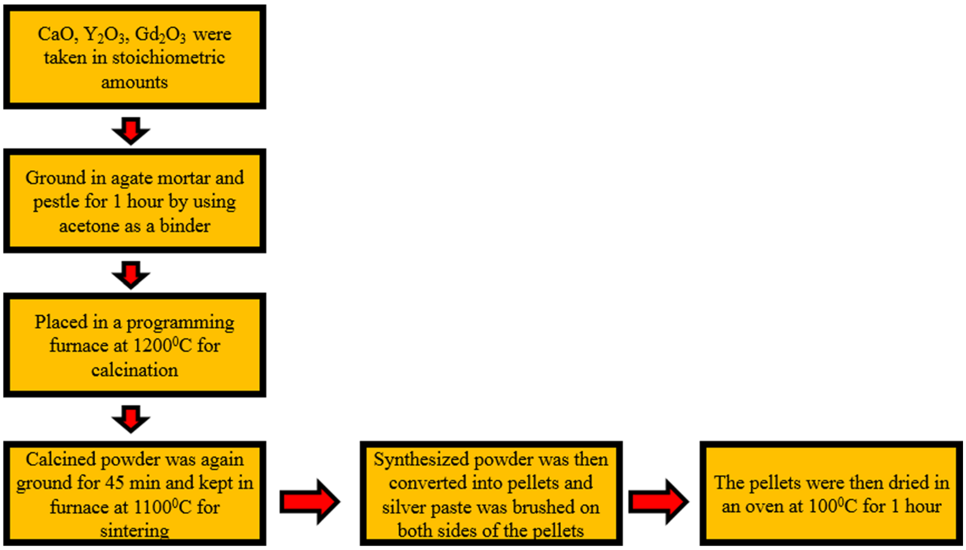

Fig. 1 Flow chart of synthesis of $Ca_{2-x}Y_2O_5$:Gd^{3+} ($x = 0$, 0.03 and 0.05 mol%) metal oxides by solid-state reaction method

Computational details

All the DFT calculations were measured using Becke's three Lee–Yang–Parr (B3LYP) hybrid GGA function [16]. Here, Def2-SVP was used as basis set along with auxiliary basis set RIJCOSX. The cubic crystal structure for $Ca_2Y_2O_5$ is − 17,136.2488 eV and wave cut-off energy is 421.32 eV. The electronic state configuration of atoms used in the calculation was Y $4p^64d^15s^2$, Ca $3d^{10}4p^65s^2$, O $2s^22p^4$. The final exchange energy E(X) was found to be − 37,660.122 eV and correlation energy E(C) was found to be − 819.378 eV with a total of E(X + C) of − 38,479.501 eV.

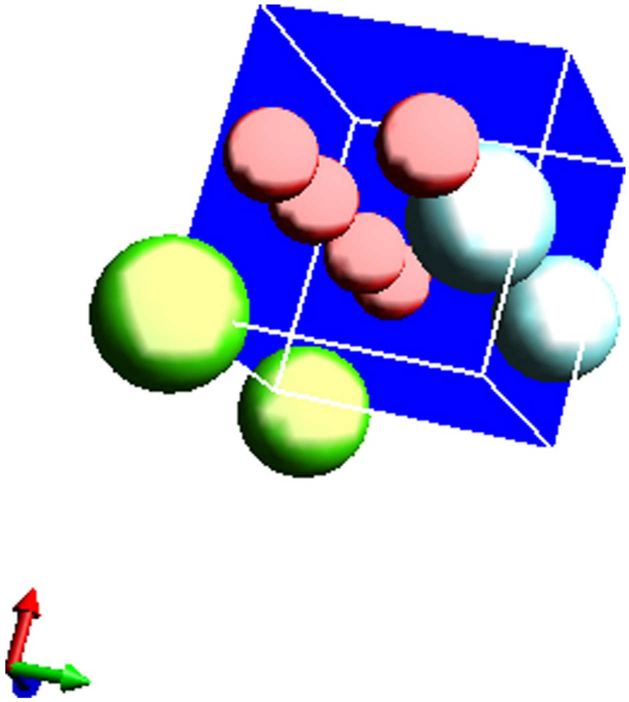

Fig. 2 Computational crystal structure for $Ca_2Y_2O_5$ metal oxide

Results and discussion

Theoretical model.

Figure 2 shows the computational crystal structure of $Ca_2Y_2O_5$ metal oxide. First-principle calculations based on DFT reveal the hexagonal crystal system with space group Ia-3, which is confirmed by previous reported results. The yttrium ions are placed at the corners of the unit cell and form a channel with calcium ions and oxygen ions. The blue balls represent yttrium element (Y), green ball is for calcium (Ca) and red ball signifies oxygen atom (O). The atomic, bond and angle properties of $Ca_2Y_2O_5$ ceramic calculated by DFT are shown in Table 1.

Electronic band structure and density of states

Using the theoretical model, the electronic band structure for $Ca_2Y_2O_5$ ceramic was computed by using B3LYP function with grid points 2 × 2 × 2 and special k-points Γ, A, K, H, M and L are given in Fig. 3. The energy gap of $Ca_2Y_2O_5$ is found to be 5 eV, confirming that it is an insulating material [24].

Figure 4 shows the graph of total density of states (DOS) versus energy for $Ca_2Y_2O_5$ ceramic respectively. DOS refers to the available number of states occupied by the system at each energy level. The maximum peaks of the ceramic move towards higher energy level with a greater number of sates for occupation. Figure 5 shows the projected density of states versus energy plot of $Ca_2Y_2O_5$ ceramic. The blue line represents the states of Ca atom, green line represents the occupation of oxygen atom and purple line shows the states of Y atom.

Table 1 Structural properties of $Ca_2Y_2O_5$ metal oxide

Element	Valence electron	X (Å)	Y (Å)	Z (Å)	Bond order	Bond length (Å)	Bond type	Bond angle (°)
Y1	2	− 2.54251	8.37417	1.82983	Sr1-O4	2.56850	O10-Y1-O17	71.8170
Ca1	2	4.90049	2.82873	0.0878	Sr1-O5	2.56843	O4-Sr1-O5	75.2984
O1	2	3.50840	3.98891	1.82983	O15-Y3	2.63408	O2-Si1-O3	110.6845
O2	1	0.80360	4.10773	1.82983	O15-Si3	1.61921	O3-Si1-Y2	79.3417
O3	1	2.12562	2.16759	0.53211	O14-Si2	1.6192	O3-Si1-O22	106.5385
Y2	3	− 1.08099	2.09808	1.82983	Si1-O2	1.64194	O1-Si1-Y2	166.2324
Ca2	2	− 0.00049	5.65832	3.66843	Y1-O17	2.51654	Si1-O1-Y3	124.311
O4	2	6.60030	3.45423	1.82983	O10-Sr2	2.53533	O9-Y3-O16	71.8170
O5	2	1.39160	4.49814	5.48948	O9-Sr2	2.53569	O13-Y4-O23	71.8173

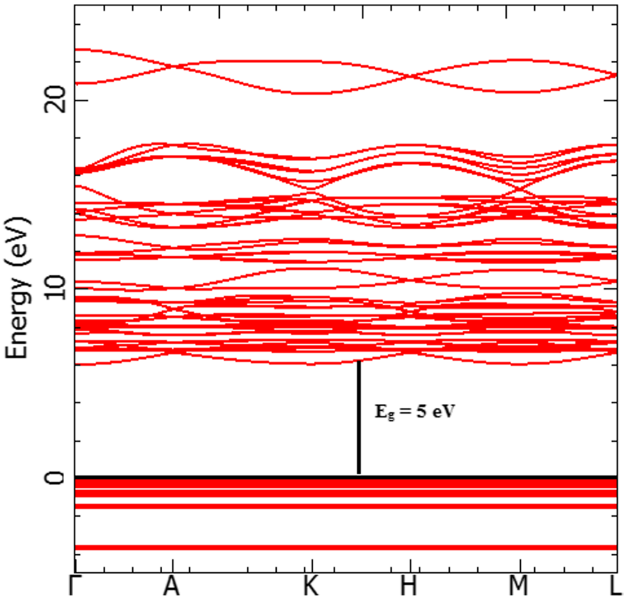

Fig. 3 Energy band structure for $Ca_2Y_2O_5$ metal oxide

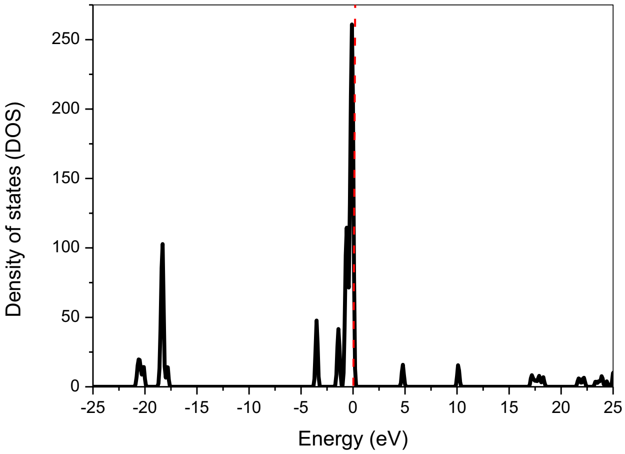

Fig. 4 Total density of states for $Ca_2Y_2O_5$ metal oxide

Mulliken population analysis

Mulliken population analysis estimates the asymmetric distribution of electronic charges along with bonding and antibonding of molecular orbitals for particular pair of atoms [25]. It is based on linear combination of molecular orbital and atomic orbital method [26]. Incorporation of defect ion changes the electronic properties of the atoms near it, so the Mulliken population of atoms and bonds adjacent to defect ion were investigated. High population value indicates the formation of covalent bond whereas low population indicates ionic bond [27].

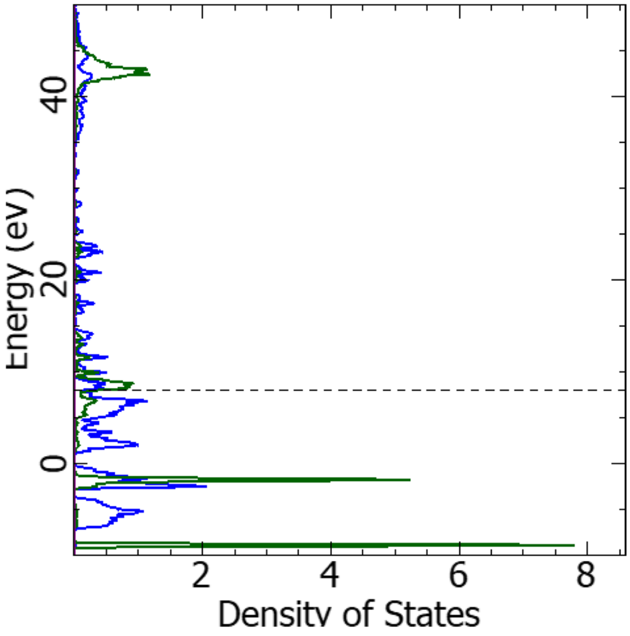

Fig. 5 Projected density of states for $Ca_2Y_2O_5$ metal oxide

The total spin and charge population of $Ca_2Y_2O_5$ ceramic is shown in Table 2. It is found that in $Ca_2Y_2O_5$, the s and p orbital of Y1 and Ca1 act as the main electron donor and loses (0.25e) and (0.111e) and d orbital of Y1 gains (0.81e).

Structural analysis.

The XRD patterns were recorded by CuK_α X-ray diffractometer in the theta range of 20–80° with a scan rate of 2°/min and step size of 0.01. The XRD pattern shown in Fig. 6 confirms the formation of single-phase cubic structure [28]. The $Ca_2Y_2O_5$ phase was confirmed by open quantum material database (OQMD) with Id—357,867. The XRD pattern shows the diffraction peaks (211), (222), (111), (400), (411), (200), (332), (134), (440), (311), (622), (220), (800), and (662). No extra peaks were observed by doping of Gd^{3+} ions in the host lattice which shows a good mixing of dopant ions in the host lattice. A slight shift in peak (222) towards higher 2θ side takes place due to the incorporation of smaller ionic radius Gd^{3+} ions (0.93 Å) to the larger ionic radius Ca^{2+} ions (0.99 Å) [29]. This causes a distortion in the cubic structure, due to which the contraction in lattice parameters takes place. The crystallite size was calculated by using the Debye–Scherer formula:

$D = 0.9\lambda/\beta cos\theta$

where β is full width half maximum and λ is X-ray wavelength.

The lattice parameters were calculated by

Table 2 Mulliken population of charge and spin for $Ca_2Y_2O_5$ metal oxide

Compound	Element	Population				Total spin	Total charge
		s	**p**	**d**	**f**		
$Ca_2Y_2O_5$	Y1	3.83 (0.21)	6.25 (0.04)	0.74 (−0.18)	0.03 (0.0002)	10.85	0.0702
	Ca1	2.45 (0.08)	6.48 (−0.03)	0.59 (0.002)	0	9.52	0.052
	O1	3.83 (−0.0002)	4.89 (−0.04)	0.003 (0.000014)	0	8.723	−0.0402

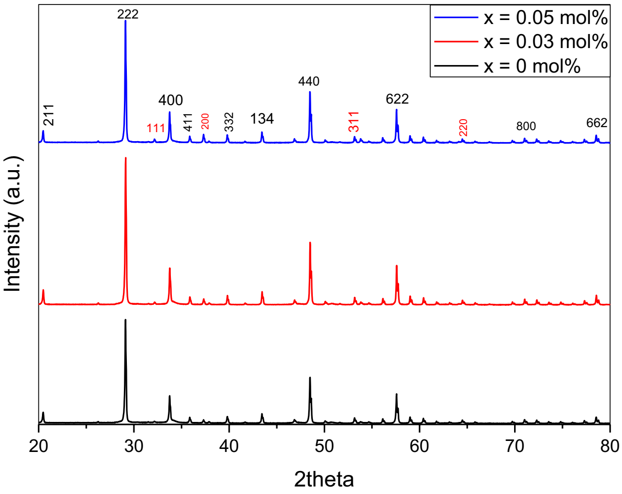

Fig. 6 X-ray diffraction patterns of $Ca_{2-x}Y_2O_5$:Gd^{3+} (x = 0, 0.03 and 0.05 mol%) metal oxides

Table 3 Calculated lattice parameters and crystallite size of $Ca_{2-x}Y_2O_5$:Gd^{3+} (x = 0, 0.03 and 0.05 mol%) metal oxides

Compound $Ca_{2-x}Y_2O_5$:xGd^{3+} with different molar concentrations (mol%)	a (Å)	b (Å)	c (Å)	Crystallite size (nm)
x = 0 mol%	2.9361	2.9361	2.9361	69.2
x = 0.03 mol%	2.9264	2.9264	2.9264	64.9
x = 0.05 mol%	2.9261	2.9261	2.9261	63.5

$$a = \lambda/2sin\theta\sqrt{h^2 + k^2 + l^2}$$

The calculated crystallite size and lattice parameters are shown in Table 3.

Morphological analysis.

The morphology of $Ca_{2-x}Y_2O_5$:xGd^{3+} (x = 0.03 mol%) sample was studied using SEM images which were recorded by ZEISS SEM analyser. The SEM images shown in Fig. 7 show the clusters of grain of irregular shape and size may be due to synthesis of metal oxide at high temperature [30]. Due to high sintering temperature, the grains get agglomerated and stick to one another and form clusters.

Dielectric studies.

When a dielectric material is placed in an electric field, the atoms or molecules rotate in the direction of the field and energy transfer takes place from the electric field into the material. The dielectric permittivity of the material is calculated by using the equation [31]

$$\varepsilon = \varepsilon_0(\varepsilon' - j\varepsilon') \quad (1)$$

where is ε_0 permittivity of free space,ε' is dielectric constant, ε" is dielectric loss and $j = \sqrt{1}$. Dielectric constant is the measure of energy stored in the dielectric material whereas

Fig. 7 Scanning electron microscopy images of magnifications (**a**) × 20,000, (**b**) × 10,000 of $Ca_{2-x}Y_2O_5$:Gd^{3+} (x = 0, 0.03 and 0.05 mol%) metal oxides

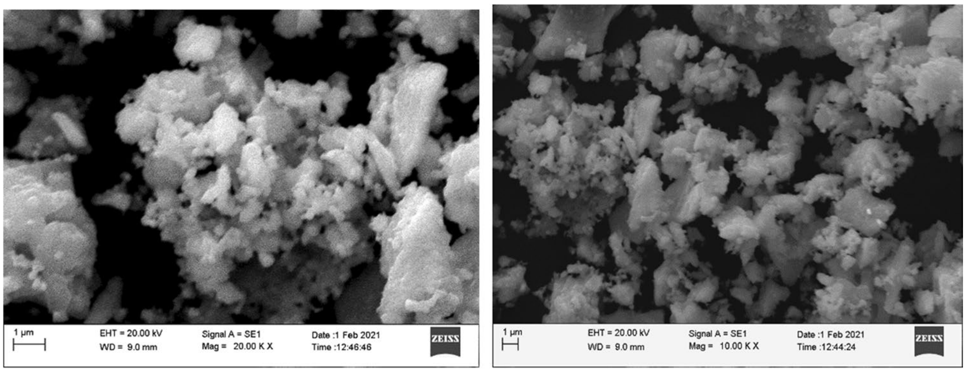

(a) (b)

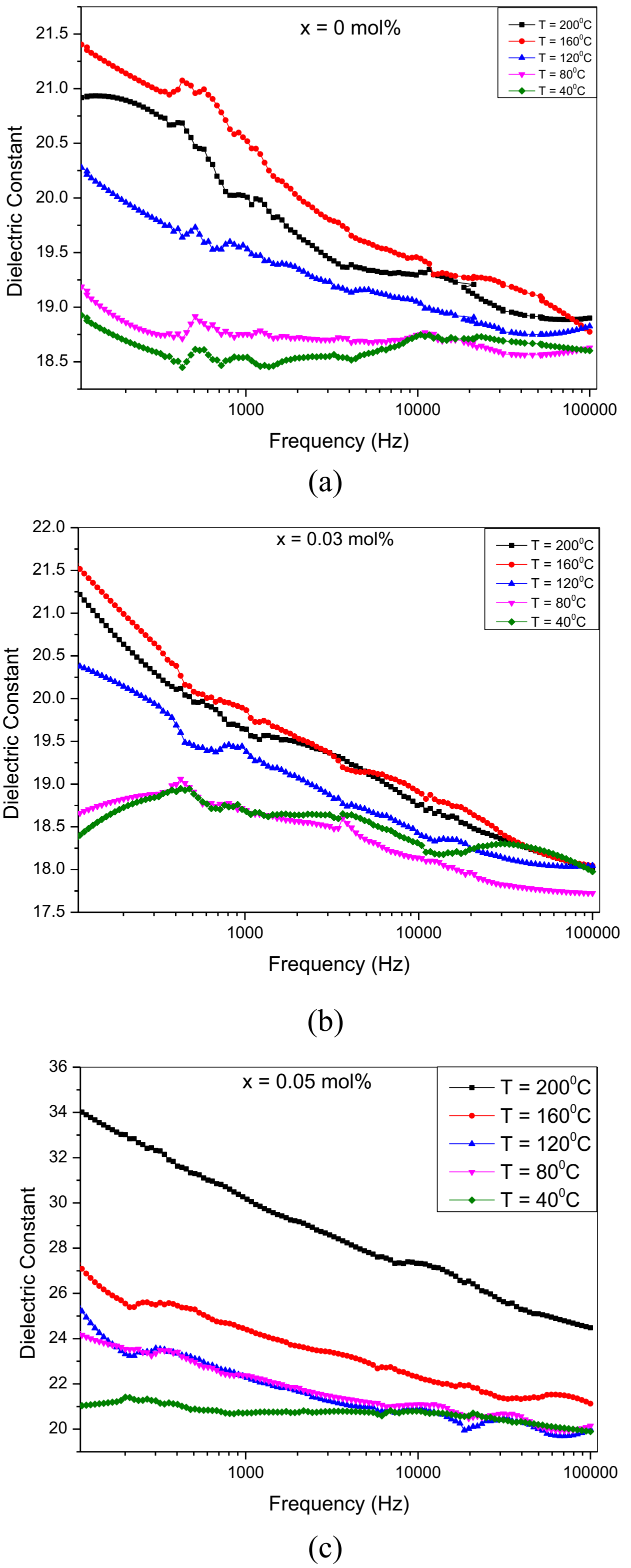

(a)

(b)

(c)

Fig. 8 Plots of dielectric constant versus frequency of $Ca_{2-x}Y_2O_5:Gd^{3+}$ metal oxides (**a**) x = 0 mol%, (**b**) x = 0.03 mol%, (**c**) x = 0.05 mol%

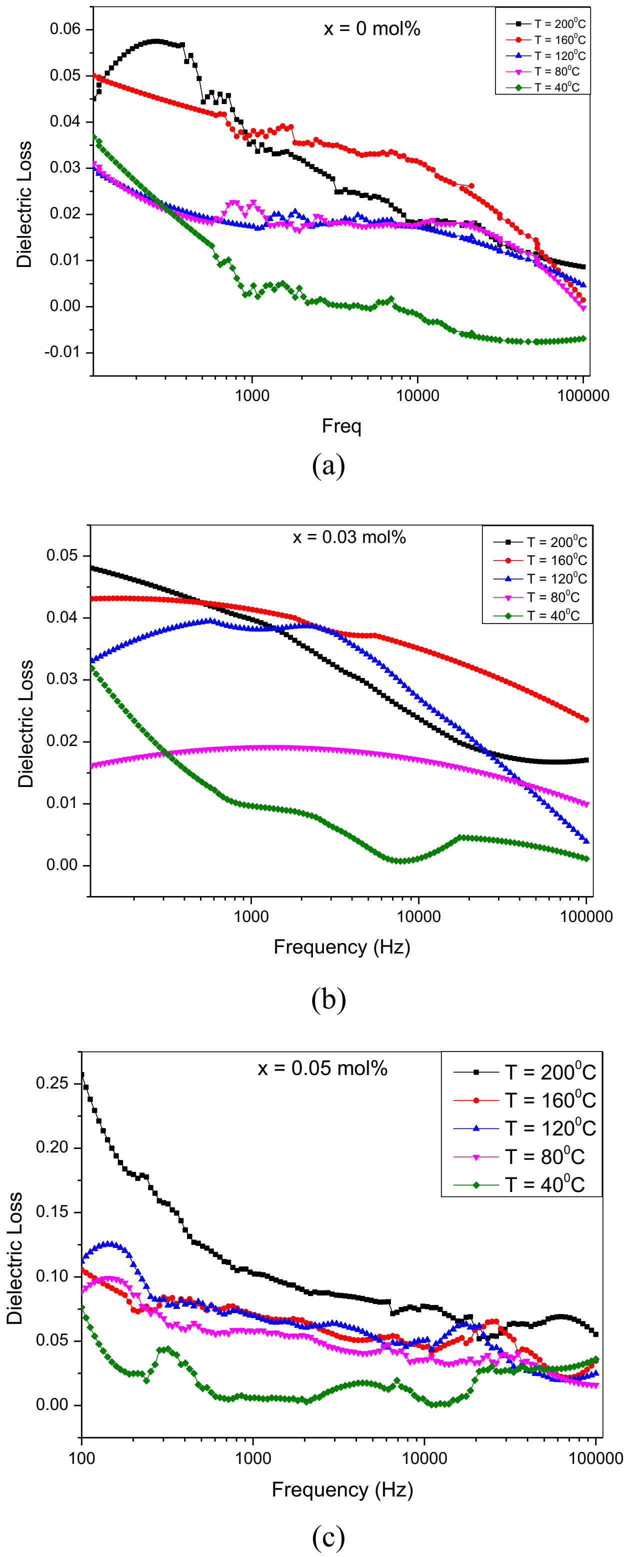

(a)

(b)

(c)

Fig. 9 Plots of dielectric loss versus frequency of $Ca_{2-x}Y_2O_5:Gd^{3+}$ metal oxides (**a**) x = 0 mol%, (**b**) x = 0.03 mol%, (**c**) x = 0.05 mol%

the amount of energy dissipated from the dielectric material is denoted by dielectric loss [32]. The loss tangent (tanδ) is the ratio of dielectric constant to dielectric loss and it is given by the expression tan δ=ε'/ε''[33].

The impedance (*Z*), capacitance (*C*), dielectric loss (*D*) and phase angle (PH) value has been taken in the frequency range 100 to 100,000 Hz. The relative permittivity or dielectric constant has been calculated by using the relation [34]

$$\varepsilon_r = \frac{Cd}{\varepsilon_0 A} \tag{2}$$

where *d* is the diameter of pellet, *A* is the area of pellet and ε_0 is permittivity of free space.

Figure 8 shows the variation of dielectric constant with frequency. The increase in dielectric constant with Gd^{3+} doping is due to space charge polarisation and rotational/orientational polarisation. In $Ca_{2-x}Y_2O_5{:}xGd^{3+}$ compounds, the oxygen vacancies act as donors and exists in the interface of nanoparticles [35]. The positive oxygen vacancies acting as hole and the negative oxygen ions pair to form dipoles and give large value of dipole moment [36]. The dipoles tend to rotate in the direction of applied field leading to the occurrence of orientational polarisation at the interface of nanoparticles [37]. A large number of defects such as porosity, vacancies and bonds are present in the compound [38]. The defects produce a change in the distribution of positive and negative ions within the interface [39]. The positive and negative charge carriers move towards the positive and negative poles of electric field giving rise to dipole moment and space charge polarisation [40].

Figure 9 shows the variation of dielectric loss with applied frequency. Dielectric loss follows the same nature as dielectric constant and decreases with the increase in frequency. The chemical bond formed between the molecules or atoms are

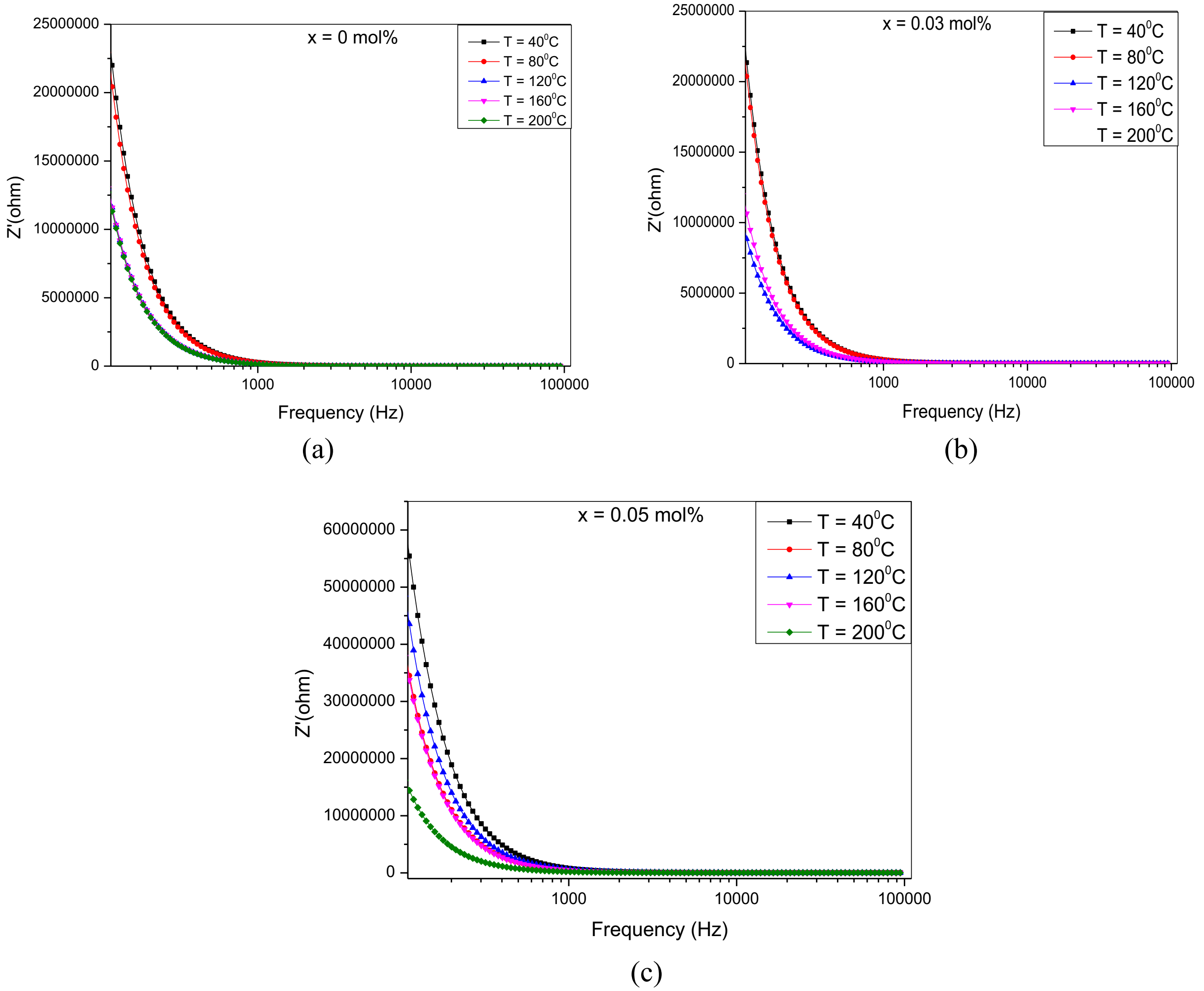

Fig. 10 Plots of real part of impedance versus frequency of $Ca_{2-x}Y_2O_5{:}Gd^{3+}$ metal oxides (**a**) x = 0 mol%, (**b**) x = 0.03 mol%, (**c**) x = 0.05 mol%

constantly changing and it changes the electronic polarisability of compounds [41]. The energy loss can take place due to defects, vacancies, breaking of bonds etc. [42].

Complex impedance studies.

Complex impedance studies over a wide range of frequency and temperature gives an idea of charge transport phenomena in the grain and grain boundary [43]. The impedance data were successfully fitted by circuit $R_g(C_gR_{gb})$ where R_g is the resistance of grain, C_g is the capacitance of grain and R_{gb} is the resistance of grain boundary.

Figure 10 shows the variation of real part of impedance (Z') with frequency. It can be seen that at lower frequency the resistance of grain and grain boundary decreases and merges in the high-frequency region due to release of space charge polarisation with increase in frequency and temperature [44]. In the low-frequency region, the charges gathered in the high-density side which leads to the increase in value of Z' [45]. As the Gd^{3+} ion concentration increases, the barrier height decreases and the charge carriers transfer from high density to low density side; as a result, Z' value decreases [46].

Figure 11 shows the variation of imaginary part of impedance (Z'') with frequency. With the increase in frequency, the value of Z'' decreases [47]. It shows the single relaxation behaviour of compound. The relaxation time is calculated by using the relation $2\pi f_{max}\tau = 1$ [48]. As the temperature rises, the dipoles rotate themselves in the direction of applied field and as a result relaxation time decreases [49].

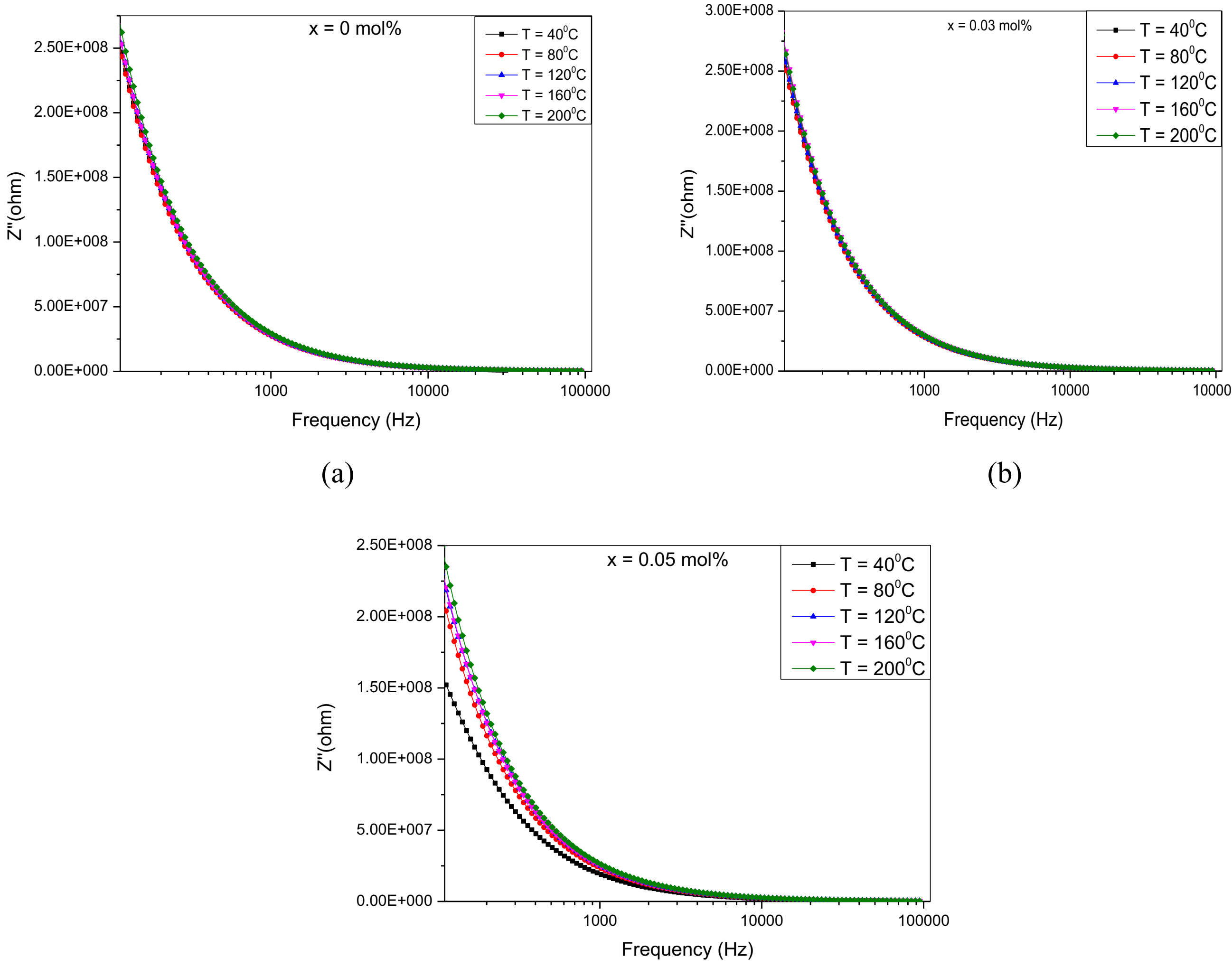

(a) (b)

(c)

Fig. 11 Plots of imaginary part of impedance versus frequency of $Ca_{2-x}Y_2O_5:Gd^{3+}$ metal oxides (**a**) x = 0 mol%, (**b**) x = 0.03 mol%, (**c**) x = 0.05 mol%

Figure 12 shows the Nyquist plots of $Ca_{2-x}Y_2O_5$:xGd^{3+} compounds. It shows the effect of R_g and R_{gb} on the compound [50]. The value of complex impedance on the lower frequency region is due to the effect of R_g whereas in the higher frequency region, it is due to R_{gb} [51]. With the increase in temperature, the resistance of grain and grain boundary decreases which shows the Debye nature of compounds [52]. The resistance of grain and grain boundary decreases with increase in Gd^{3+} ion concentration which shows an increase in the value of electrical conductivity [53].

Electrical modulus spectroscopy.

The electrical modulus spectroscopy reveals the hopping mechanism of charge carriers between the cationic and anionic sites [54]. The main advantage of modulus spectroscopy is that the electrode effect is suppressed in this spectroscopy [55]. The inhomogeneous nature of compound can be easily depicted by using electrical modulus spectroscopy [56]. The real and imaginary part of modulus can be calculated by using the equation [57]

$$M' = \omega C_0 Z''$$

$$M'' = \omega C_0 Z'$$

Figure 13 shows the variation of real part of modulus (M') with frequency. In the low-frequency region, the value of M' is almost constant due to short range motion of charge carriers [58]. With the increase in frequency, the value of M' increases due to long-range hopping of charge carriers [59]. The short-range motion of charge carriers is due to lack of

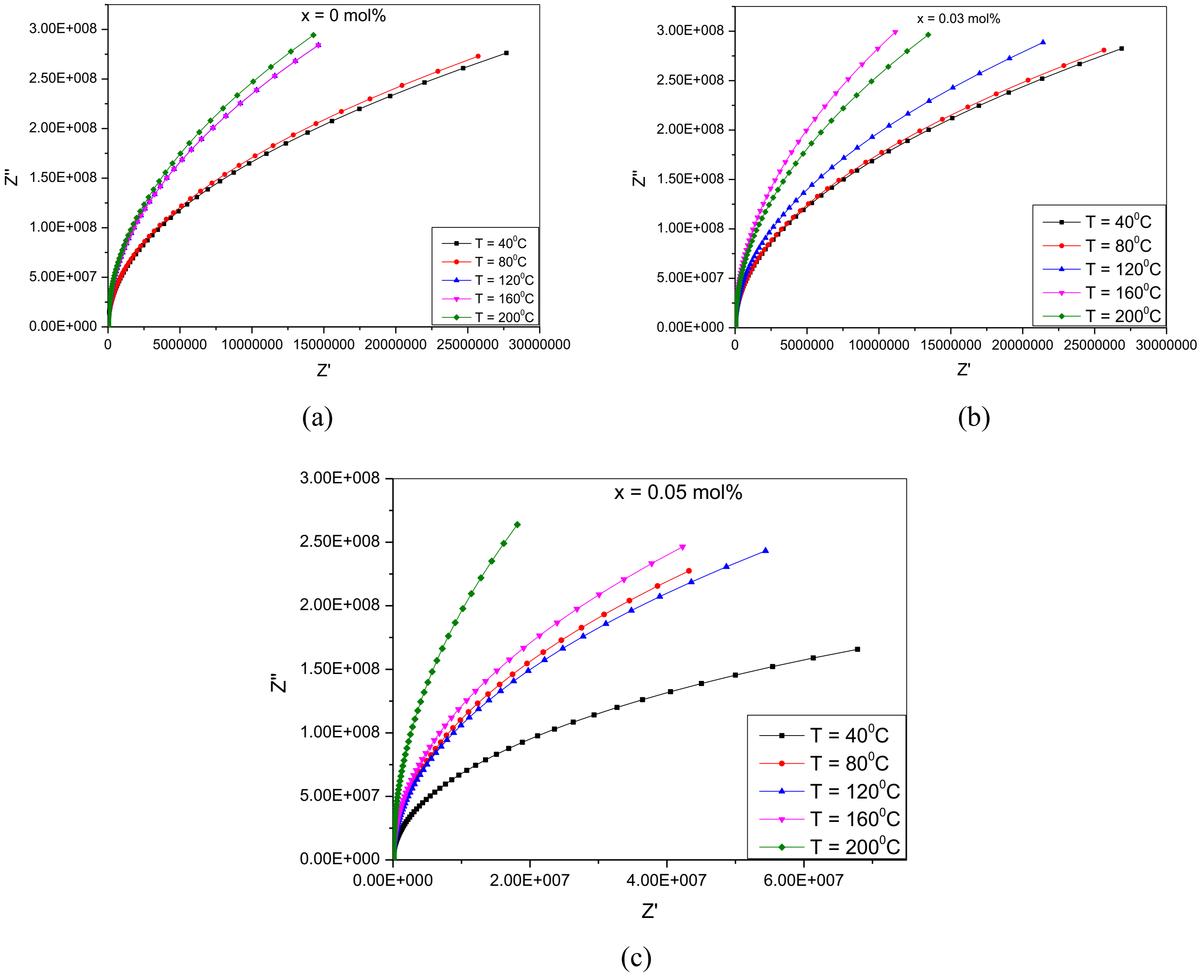

(a)

(b)

(c)

Fig. 12 Nyquist plots of $Ca_{2-x}Y_2O_5$:Gd^{3+} metal oxides (**a**) x = 0 mol%, (**b**) x = 0.03 mol%, (**c**) x = 0.05 mol%

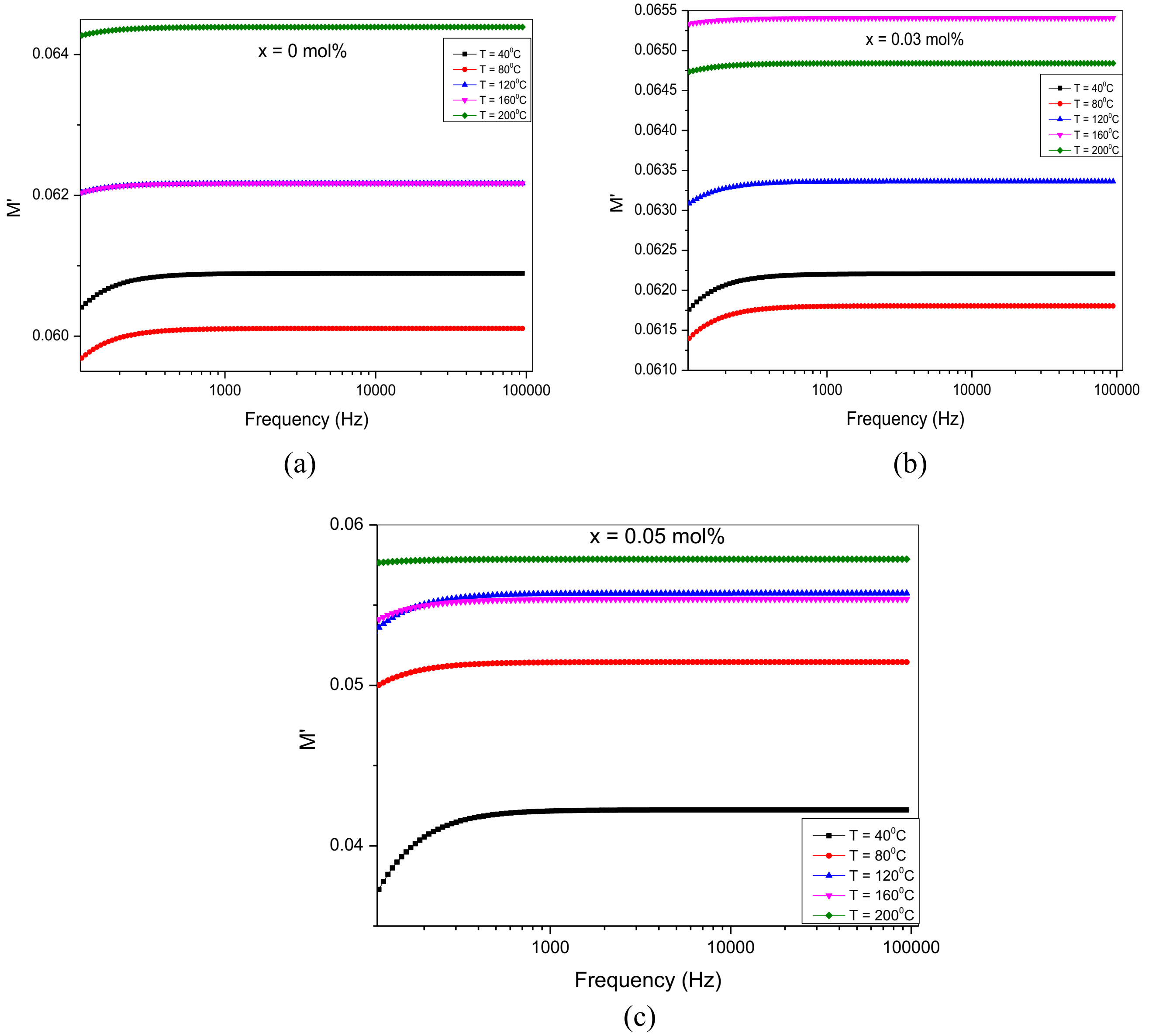

(a) (b) (c)

Fig. 13 Plots of real part of modulus versus frequency of $Ca_{2-x}Y_2O_5:Gd^{3+}$ metal oxides (**a**) x = 0 mol%, (**b**) x = 0.03 mol%, (**c**) x = 0.05 mol%

restoring force required for the motion of charge carriers in the presence of electric field [60].

Figure 14 shows the variation of imaginary part of modulus with applied frequency. A relaxation behaviour is observed at higher frequency side with the increase in temperature due to the motion of immobile ions [61]. In the lower frequency region, the value of M'' increases due to long range motion of charge carriers [62]. With the further increase in frequency, the motion of charge carrier decreases, due to which a decrease in the value of M'' was observed [63].

Electrical conductivity study.

The AC conductivity analysis gives information about the electrical behaviour of the compounds [64]. Figure 15 shows the plots of AC conductivity versus frequency for $Ca_{2-x}Y_2O_5:xGd^{3+}$ compounds at different temperatures.

The electrical conduction behaviour was explained by Jonscher using the universal power law [65]:

$$\sigma_{ac} = \sigma_{dc} + A\omega^n$$

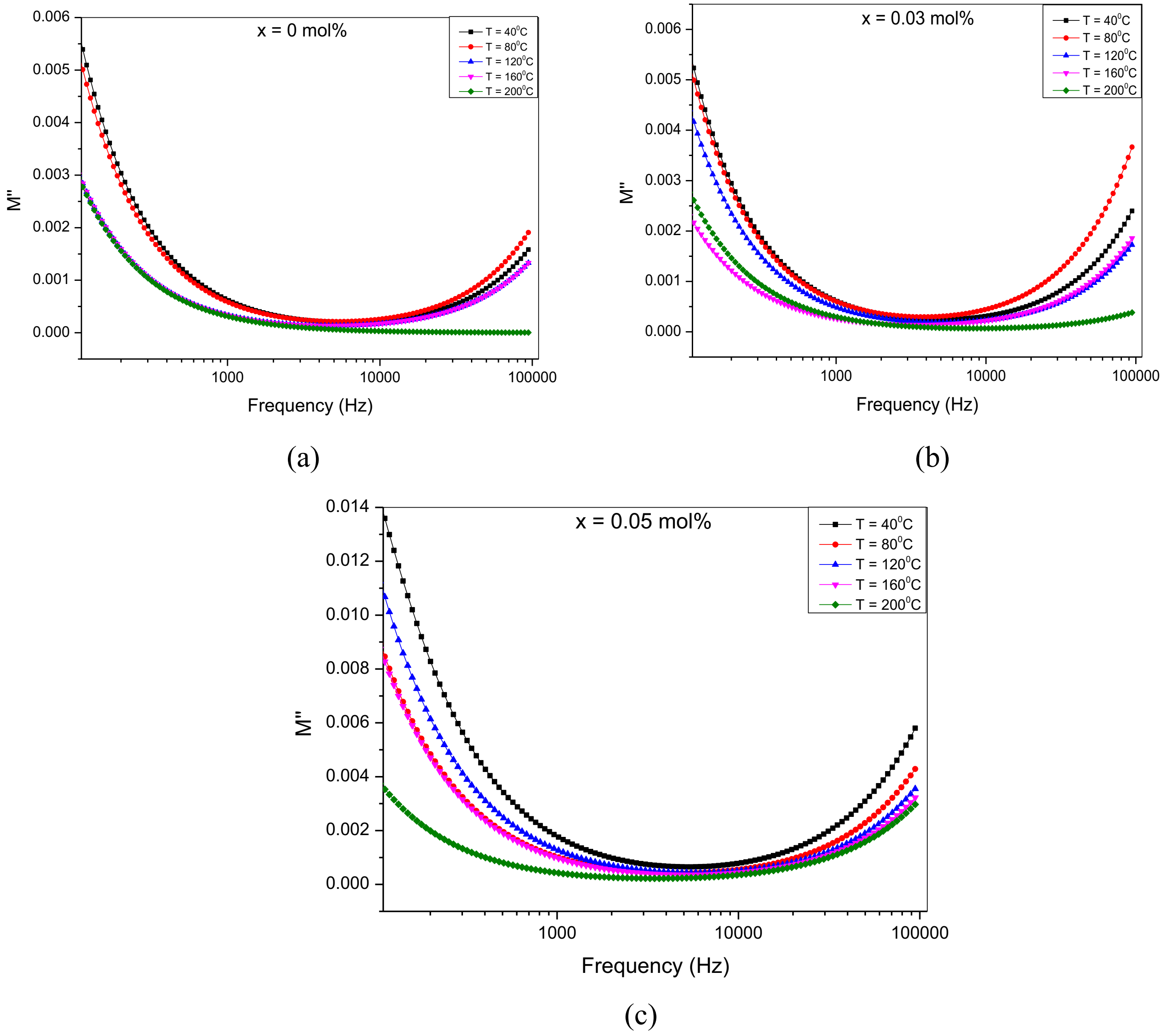

Fig. 14 Plots of imaginary part of modulus versus frequency of $Ca_{2-x}Y_2O_5:Gd^{3+}$ metal oxides (**a**) x = 0 mol%, (**b**) x = 0.03 mol%, (**c**) x = 0.05 mol%

where σ_{dc} is the frequency independent conductivity, A is the temperature-dependent term, ω is the frequency and the value of n describes the hopping mechanism in the low- and high-frequency region. The value of n $(0 < n < 1)$ corresponds to translational hopping of charge carriers; however, $(1 < n < 2)$ shows the localised orientational hopping mechanism. In the low-frequency region, the AC conductivity is frequency independent whereas the change in slope of AC conductivity is observed in the high-frequency region [66]. The frequency at which the change in slope takes place is known as hopping frequency (ω_p) [67]. The change in slope takes place due to the polaron hopping of charge carriers with rise in temperature [68]. By increasing the temperature, the ω_p shift towards higher frequency region and it depends on the dopant concentration in metal oxide [69]. Table 4 shows the value of n for different temperatures and molar concentrations for $Ca_{2-x}Y_2O_5:xGd^{3+}$ compounds. The prepared undoped ceramic is an insulator, but it shows some conductivity due to the presence of oxygen interstitials.

Conclusion

The $Ca_{2-x}Y_2O_5:Gd^{3+}$ (x = 0, 0.03 and 0.05 mol%) metal oxides were synthesised by solid-state reaction method. Crystal structure computed theoretically shows a good

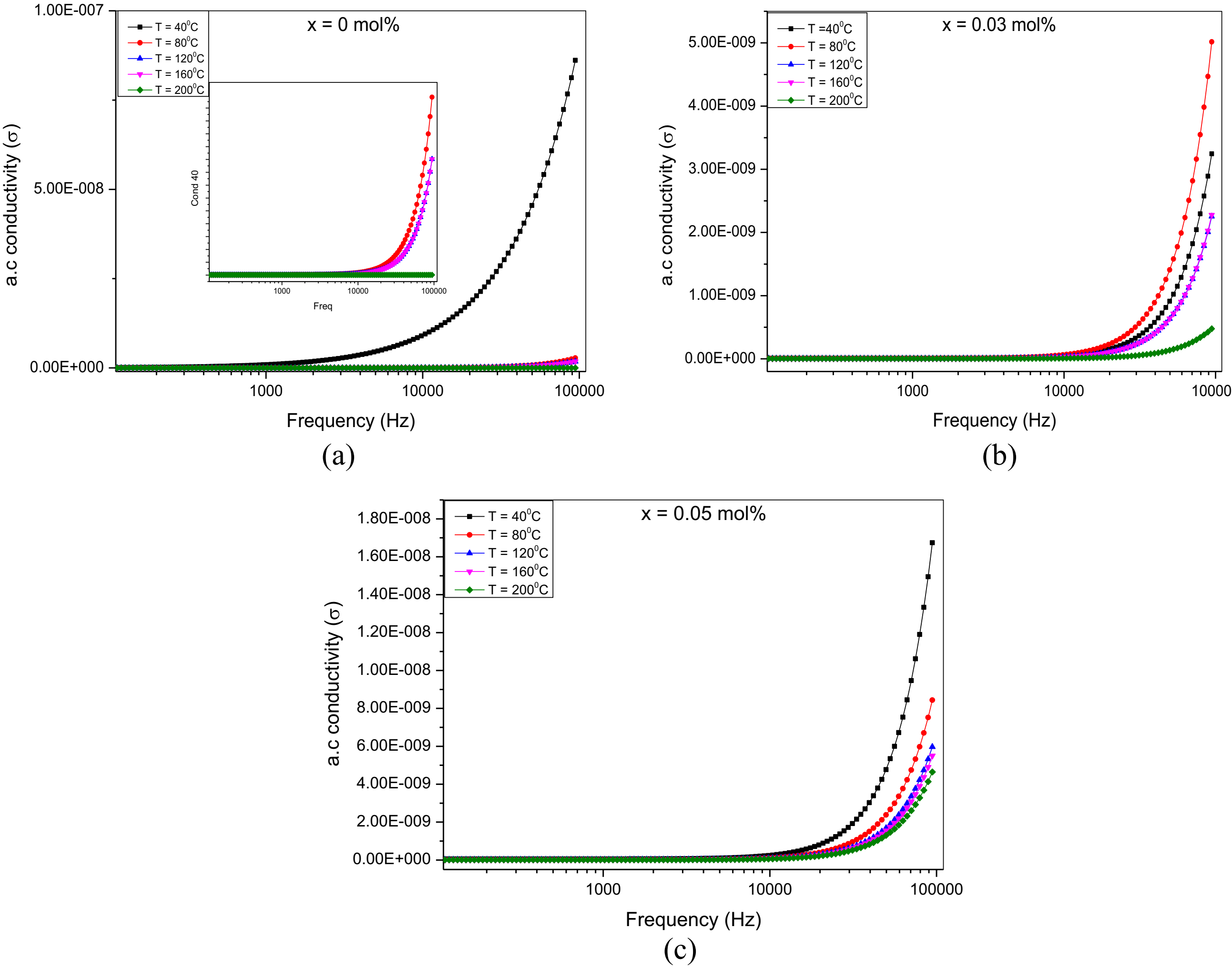

(a) (b) (c)

Fig. 15 Plots of AC conductivity versus frequency of $Ca_{2-x}Y_2O_5:Gd^{3+}$ metal oxides (**a**) x = 0 mol%, (**b**) x = 0.03 mol%, (**c**) x = 0.05 mol%

Table 4 Calculated integer (*n*) value of $Ca_{2-x}Y_2O_5:Gd^{3+}$ (x = 0, 0.03 and 0.05 mol%) metal oxides

Molar concentration (x) (mol%)	Temperature (°C)	*n*
x = 0	40	1.01
	80	1.03
	120	1.14
	160	1.22
	200	1.23
x = 0.03	40	1.02
	80	1.10
	120	1.25
	160	1.28
	200	1.30
x = 0.05	40	1.18
	80	1.20
	120	1.22
	160	1.25
	200	1.26

agreement with experimental crystallographic analysis. The formation of cubic structure along with space group Ia-3 of the metal oxides has been confirmed from both the theoretical and experimental analyses. DFT-based, first-principle calculations of $Ca_2Y_2O_5$ ceramic reveal that the value of energy gap is 5 eV. The formation of clusters of grain of irregular shape and size was confirmed from scanning electron microscopy images. Dielectric constant and dielectric loss decrease with the increase in frequency which confirms that space charge and orientational polarisations are dominant mechanisms in the high-frequency region. Complex impedance spectroscopy reveals the Debye nature of the synthesised metal oxides. Electrical modulus spectroscopy shows the transport of charge carriers between Ca^{2+} and O^{2-} ions. Electrical conductivity analysis depicts that the conduction mechanism is through small polaron hopping. The prepared metal oxides follow Jonscher's power law and can have application in microelectronic devices.

Declarations

Conflict of interest The author declares no competing interests.

References

1. Bredar, A.R.C., Chown, A.L., Burton, A.R., Farnum, B.H.: Electrochemical impedance spectroscopy of metal oxide electrodes for energy applications. ACS Appl. Energy Mater. **3**, 66–98 (2020). https://doi.org/10.1021/acsaem.9b01965
2. Bansal, N.P.: Influence of several metal ions on the gelation activation energy of silicon tetraethoxide. J. Ame. Cera. Soc. **73**, 2647–2652 (1990). https://doi.org/10.1111/j.1151-2916.1990.tb06741.x
3. Kuwabara, M., Ide, T.: CO gas sensitivity in porous semiconducting barium–titanate ceramics. Am. Ceram. Soc. Bull. **66**, 1401–1405 (1987)
4. Chiu, C.M., Chang, Y.H.: The structure, electrical and sensing properties for CO of the La0.8Sr0.2Co1 − xNixO3 − δ system. Materials Science and Engineering A **266**, 93–98 (1999)
5. Joseph, B., Gopchandran, K.G., Manoj, P.K.: Optical and electrical properties of zinc oxide films prepared by spray pyrolysis. Bull. Mater. Sci. **22**, 921–926 (1999)
6. Dayan, N.J., Sainkar, S.R., Karekar, R.N.: Formulation and characterization of ZnO: Sb thick-film gas sensors. Thin Solid Films **325**, 254–258 (1998)
7. Krishnan, B., Nampoori, V.P.N.: Screen printed nanosized ZnO thick film. Bull. Mater. Sci. **28**, 239–242 (2005)
8. Som, S., Sharma, S.K.: Eu3+/Tb3+-codoped Y2O3 nanophosphors: Rietveld refinement, bandgap and photoluminescence optimization. J. Phys. D Appl. Phys. **45**, 415102 (2012). https://doi.org/10.1088/0022-3727/45/41/415102
9. Qian, C., Zeng, T., Liu, H.: Synthesis and downconversion emission property of Yb2O3:Eu3+ nanosheets and nanotubes. Adv. Condens. Matter. Phys. **519869,** 1–5(2013). https://doi.org/10.1155/2013/519869
10. Srinivasan, M.P., Punithavelan, N.: Structural, morphological and dielectric investigations on NiO/CuO/ZnO combined semiconductor metal oxide structures based ternary nanocomposites. Mater. Res. Express **5**, 075033 (2018)
11. Mohamed, M.B., Sayed, K.E.: Structural, magnetic and dielectric properties of (PANI)–Ni0.5Zn0.5Fe1.5Cr0.5O4 nanocomposite. Composites Part B: Engineering **56**, 270–278 (2014). https://doi.org/10.1016/j.compositesb.2013.08.038
12. Saxena, P., Choudhary, P., Yadav, A.: Effect of transition metal substitution on structural and dielectric properties of Mg0.5Zn0.5−xCrxCo2O4 (0.0 ≤ x ≤ 0.5) cobaltite. J Mater Sci: Mater Electron **30**, 7292–7300 (2019). https://doi.org/10.1007/s10854-019-01042-4
13. Lakhane, M., Bogle, K., Khairnar, R., Dahiwale, S., Sharma, R., Mokale, V., Mahabole, M.: Dielectric properties of zeolite based metal oxide nanocomposites. Nano-Structures & Nano-Objects **17**, 248–258 (2019). https://doi.org/10.1016/j.nanoso.2019.01.008
14. Tack, L.W., Azam, M.A., Seman, R.N.A.R.: Structural and electronic properties of transition-metal oxides attached to a single-walled CNT as a lithium-ion battery electrode: a first-principles study. J. Phys. Chem. A **121**, 2636–2642 (2017). https://doi.org/10.1021/acs.jpca.6b12904
15. Skorodumova, N.V., Hermansson, K., Johansson, B.: Structural and electronic properties of the (100) surface and bulk of alkaline-earth metal oxides. Phys. Rev. B **72**, 125414 (2005). https://doi.org/10.1103/PhysRevB.72.125414
16. Robertson, J.: High dielectric constant oxides. Eur. Phys. J. Appl. Phys. **28**, 265–291 (2004). https://doi.org/10.1051/epjap:2004206
17. Dong, M., Wang, H., Ye, C., Shen, L., Wang, Y., Zhang, J., Ye, Y.: Structure and electrical properties of sputtered TiO2/ZrO2 bilayer composite dielectrics upon annealing in nitrogen. Nanoscale Res. Lett. **7**, 1–5 (2012). http://www.nanoscalereslett.com/content/7/1/31
18. Choi, C., Lee, K.L., Narayanan, V.: Impact of diffusion less anneal using dynamic surface anneal on the electrical properties of a high-k/metal gate stack in metal-oxide-semiconductor devices. Appl. Phys. Lett. **98**, 123506 (2011)
19. Das, T., Mahata, C., Maiti, C.K., Miranda, E., Sutradhar, G., Bose, P.K.: Effects of Ti incorporation on the interface properties and band alignment of HfTaOx thin films on sulfur passivated GaAs. Appl. Phys. Lett. **98**, 022901 (2011)
20. Khomenkova, L., Portier, X., Marie, P., Gourbilleau, F.: Hafnium silicate dielectrics fabricated by RF magnetron sputtering. J. Non. Cryst. Solids **357**, 1860 (2011)
21. Feng, X.Y., Shen, C., Fang, X., Chen, C.H.: Synthesis of LiNi0.5Mn1.5O4 by solid-state reaction with improved electrochemical performance. J. All. Comp. **509**, 3623–3626 (2011). https://doi.org/10.1016/j.jallcom.2010.12.116
22. Parhi, P., Karthik, T.N., Manivannan, V.: Synthesis and characterization of metal tungstates by novel solid-state metathetic approach. J. All. Comp. **465**, 380–386 (2008). https://doi.org/10.1016/j.jallcom.2007.10.089
23. Damien, B., Fabienne, A., Thibault, C., Dimitri, S., Didier, B.A.: Solid-state synthesis of monazite-type compounds $LnPO_4$ (Ln = La to Gd). Sol. Stat. Sci. **9**, 432–439 (2007). https://doi.org/10.1016/j.solidstatesciences.2007.03.019
24. Hohenberg, P., Kohn, W.: Inhomogeneous electron gas. Phys. Rev. **136**, 1–8 (1964). https://doi.org/10.1103/PhysRev.136.B864
25. Rulis, P., Ouyang, L., Ching, W.Y.: Electronic structure and bonding in calcium apatite crystals: hydroxyapatite, fluorapatite, chlorapatite, and bromapatite. Phys. Rev. B **70**, 155104 (2004). https://doi.org/10.1103/PhysRevB.70.155104
26. Roy, R.K., Hirao, K., Krishnamurty, S., Pal, S.: Mulliken population analysis based evaluation of condensed Fukui function indices using fractional molecular charge. Journal of chemical physics **11**, 2901–2907 (2001). https://doi.org/10.1063/1.1386699
27. Jeria, J.S.G.: An empirical way to correct some drawbacks of Mulliken population analysis. J. Chil. Chem. Soc. **54**, 482–485 (2009)
28. Stuchebrukhov, A.A.: Tunnelling currents in proteins: non-orthogonal atomic basis sets and Mulliken population analysis. J. Chem. Phys. **107**, 6495–6498 (1997). https://doi.org/10.1063/1.474308
29. Gnanasekaran, L., Hemamalini, R., Saravanan, R., Ravichandran, K., Gracia, F., Agarwal, S., Gupta, V.K.: Synthesis and characterization of metal oxides (CeO2, CuO, NiO, Mn3O4, SnO2 and ZnO) nanoparticles as photo catalysts for degradation of textile dyes. J. Photochem. & Photobio. B: Biology **173**, 43–49 (2017). https://doi.org/10.1016/j.jphotobiol.2017.05.027
30. Sudha, V., Murugadoss, G., Thangamuthu, R.: Structural and morphological tuning of Cu-based metal oxide nanoparticles by a facile chemical method and highly electrochemical sensing of sulphite. Sci Rep **11**, 3431 (2021). https://doi.org/10.1038/s41598-021-82741-z
31. Landers, J., Ortiz, J.C., Zong, K., Goswami, A., Asefa, T., Vishnyakov, A., Neimark, A.V.: In situ growth and characterization of metal oxide nanoparticles within polyelectrolyte membranes. Wiley VCH (2016). https://doi.org/10.1002/anie.201606178
32. Hong, X., Liao, L.: Solution Processed Metal Oxide Thin Films for Electronic Applications. Metal Oxides Series **1**, 31–39 (2020). https://doi.org/10.1016/B978-0-12-814930-0.00003-7

33. Li, H., Han, D., Dong, J., Yu, W., Liang, Y., Luo, Z., Zhang, S., Zhang, X., Wang, Y.: Enhanced electrical properties of dual-layer channel ZnO thin film transistors prepared by atomic layer deposition. Appl. Surf. Sci. **439**, 632–637 (2018). https://doi.org/10.1016/j.apsusc.2017.12.234
34. Ruan, D.B., Liu, P.T., Gan, K.J., Chiu, Y.C., Yu, M.C., Chien, T.C., Chen, Y.H., YiKuo, P., Sze, S.M.: The influence on electrical characteristics of amorphous indium tungsten oxide thin film transistors with multi-stacked active layer structure. Thin Sol. Films **666**, 94–99 (2018). https://doi.org/10.1016/j.tsf.2018.09.005
35. Yang, J., Hu, Y., Jin, C., Zhuge, L.: Xuemei Wu, Structural and optical properties of Er-doped TiO2 thin films prepared by dual-frequency magnetron co-sputtering. Thin Solid Films **637**, 9–13 (2017). https://doi.org/10.1016/j.tsf.2017.03.012
36. Salama, A.H., Abdel-Karim, A.M.: Synthesis, characterization and dielectric properties of novel metal oxide–phthalocyanine nanocomposites. Egypt. J. Chem. **61**, 281–294 (2018)
37. Guo, Z., Liu, A., Meng, Y., Fan, C., Shin, B., Liu, G., Shan, F.: Solution-processed ytterbium oxide dielectrics for low-voltage thin-film transistors and inverters. Ceramics Int. **43**, 15194–15200 (2017). https://doi.org/10.1016/j.ceramint.2017.08.052
38. Kumar, A., Mondal, S., Rao, K.S.R.K.: Low temperature solution processed high-κ ZrO_2 gate dielectrics for nanoelectonics. Appl. Sur. Sci. **370**, 373–379 (2016). https://doi.org/10.1016/j.apsusc.2016.02.176
39. Zhang, Q., Xia, G., Xia, W., Zhou, J., Wang, S.: Low-temperature solution-processed high-k ZrTiOx dielectric films for high-performance organic thin film transistors. Synth. Met. **210**, 282–287 (2015). https://doi.org/10.1016/j.synthmet.2015.10.011
40. Abdullah, M.M.: Facile growth, physical characterization, and dielectric response of as-grown NiO nanostructures. J. King Saud Uni. **32**, 1048–1054 (2020). https://doi.org/10.1016/j.jksus.2019.09.009
41. Perumal, R., Thanikaikarasan, S.: Thickness, structural and optical properties of electrodeposited NiO thin films. Materials Today: Proceedings **33**, 3989–3992 (2020). https://doi.org/10.1016/j.matpr.2020.06.337
42. Lanje, A.S., Sharma, S.J., Ningthoujam, R.S., Ahn, J.S., Pode, R.B.: Low temperature dielectric studies of zinc oxide (ZnO) nanoparticles prepared by precipitation method. Advanced Powder Tech. **24**, 331–335 (2013). https://doi.org/10.1016/j.apt.2012.08.005
43. Rai, P., Yu, Y.T.: Citrate-assisted hydrothermal synthesis of single crystalline ZnO nanoparticles for gas sensor application. Sens. & Actu. B: Chem. **173**, 58–65 (2012). https://doi.org/10.1016/j.snb.2012.05.068
44. Ameen, S., Akhtar, M.S., Song, M., Shin, H.S.: Metal oxide nanomaterials, conducting polymers and their nanocomposites for solar energy. InTech Open **1**, 203–259 (2013). https://doi.org/10.5772/51432
45. Skotheim, T.A., Reynolds, J.R.: Handbook of Conducting Polymers: Conjugated Polym. CRC Press, Boca Raton (2007)
46. Hossen, M.B., Hossain, A.K.M.A.: Complex impedance and electric modulus studies of magnetic ceramic Ni0.27Cu0.10Zn0.63Fe2O4. J. Adv. Ceram. **4**, 217–225 (2015). https://doi.org/10.1007/s40145-015-0152-2
47. Kumar, A., Singh, B.P., Choudhary, R.N.P., Thakur, A.K.: Characterization of electrical properties of Pb-modified BaSnO3 using impedance spectroscopy. Mater. Chem. Phys. 99, 150–159 (2006).https://doi.org/10.1016/j.matchemphys.2005.09.086
48. Das, P.S., Chakraborty, P.K., Behera, B., Mohanty, N.K., Choudhary, R.N.P.: Impedance spectroscopy study of Na2SmV5O15 ceramics. J. Adv. Ceram. 3, 1–6 (2014). https://doi.org/10.1007/s40145-014-0087-z
49. Lanfredi, S., Nobre, M.A.D.L.: Dielectric dispersion in Bi3 Zn2 Sb3 O14 ceramic: a pyrochlore type phase. Mat. Res. 6 (2003) 157–161,10.1590/ S1516-14392003000200008.[39] D.C. Sinclair, A.R. West, Impedance and modulus spectroscopy of semiconducting BaTiO3 showing positive temperature coefficient of resistance. J. Appl. Phys.66, 3850–3857 (1989).https://doi.org/10.1063/1.344049
50. Płcharski, J., Weiczorek, W.: PEO based composite solid electrolyte containing nasicon. Solid State Ionics 28,979–982 (1988).https://doi.org/10.1016/0167-2738(88)90315-3
51. Singh, H., Kumar, A., Yadav, K.L.: Structural, dielectric, magnetic, magnetodielectric and impedance spectroscopic studies of multiferroic BiFeO3–BaTiO3 ceramics. Mater. Sci. Eng. 176, 540–547 (2011). https://doi.org/10.1016/j.mseb.2011.01.010
52. Beg, S., Areqi, N.A.S.A., Haneef, S.: Haneef, Study of phase transition and ionic conductivity changes of Cd-substituted Bi4V2O11 – δ. Solid State Ionics 179, 2260–2264 (2008).https://doi.org/10.1016/j.ssi.2008.08.008
53. Dasari, M.P., Godavarti, U., Mote, V.: Structural, morphological, magnetic and electrical properties of Ni-doped ZnO nanoparticles synthesized by co-precipitation method. Process. Appl. Ceram **12**, 100–110 (2018). https://doi.org/10.2298/PAC1802100D
54. Roling, B.: Scaling properties of the conductivity spectra of glasses and super cooled melts. Solid State Ionics 105, 185–193 (1998).https://doi.org/10.1016/S0167-2738(97)00463-3
55. Liu, J., Duan, C.G., Yin, W.G., Mei, W.N., et al.: Dielectric permittivity and electric modulus in Bi2Ti4O11. J. Chem. Phys. 119, 2812–2819 (2003).https://doi.org/10.1063/1.1587685
56. Bag, S., Das, P., Behera, B.: AC impedance spectroscopy and conductivity studies of Dy doped Bi4V2O11 ceramics. J. Theor. Appl. Phys. 11, 13–25 (2017). https://doi.org/10.1007/s40094-017-0246-z
57. Shamim, M.K., Sharma, S., Sinha, S., Nasreen, E.: Dielectric relaxation and modulus spectroscopy analysis of (Na0:47 K0:47 Li0:06) NbO3 ceramics. J. Adv. Dielectr. 7, 1750020–1750031 (2017).https://doi.org/10.1142/S2010135X17500205
58. Richert, R., Wagner, H.: The dielectric modulus: relaxation versus retardation. Solid State Ionics 105,167–173 (1998)
59. Tsangaris, G.M., Psarras, G.C., Kouloumbi, N.: Electric modulus and interfacial polarization in composite polymeric systems. J. Mat. SCI. 33, 2027–2037 (1998)
60. Behera, B., Nayak, P., Choudhary, R.N.P.: Studies of dielectric and impedance properties of KCa2V5O15 ceramics. J. Phy & Chem. Solids 69, 1990–1995 (2008).https://doi.org/10.1016/j.jpcs.2008.02.013
61. Barik, S.K., Mahapatra, P.K., Choudhary, R.N.P.: Structural and electrical properties of Na1/2La1/2TiO3 ceramics. Appl. Phys. A **11**, 199–203 (2006). https://doi.org/10.1007/s00339-006-3668-z.
62. Cao, M.S., Hou, Z.L., Yuan, J., Xiong, L.T., Shi, X.L.: Low dielectric loss and non-Debye relaxation of gamma-Y2Si2O7 ceramic at elevated temperature in X-band. J. Appl. Phys.105, 106102 (2009).https://doi.org/10.1063/1.3117525
63. Cao, M.S., Hou, Z.L., Yuan, J., et al.: The effects of temperature and frequency on the dielectric properties, electromagnetic interference shielding and microwave-absorption of short carbon fiber/silica composites. Carbon 48, 788–796 (2010).https://doi.org/10.1016/j.carbon.2009.10.028
64. Özdemir, Z.G., Kılıç, M., Karabul, Y.S., Erd¨onmez, S., Içelli, O.: The influence of the partially europium substitution on the AC electrical properties of BiSr2CaCu2O6.5 ceramics. Process. Appl. Ceram. 13, 323–332 (2019). https://doi.org/10.2298/PAC1904323O
65. Jonscher, A.K.: The ‘universal’dielectric response. Nature 267, 673–679 (1977).https://doi.org/10.1109/CEIDP.1990.201316

66. Funke, K.: Jump relaxation in solid electrolytes. Prog. Solid State Chem. 22, 111–195 (1993).https://doi.org/10.1016/0079-6786(93)90002-9
67. Elliot, S.R.: A.c. conduction in amorphous chalcogenide and pnictide semiconductors. Adv. Phys. 36, 135–217 (1987).https://doi.org/10.1080/00018738700101971
68. Roy, A.K., Singh, A., Kumari, K., Nath, K.A., Prasad, A., Prasad, K.: Electrical properties and AC conductivity of (Bi0.5Na0.5)0.94Ba0.06TiO3 ceramic. ISRN Ceramics 2012, 854831–854841 (2012).https://doi.org/10.5402/2012/854831
69. Maldzius, R., Sirviö, P., Sidaravicius, J., Lozovski, T., Backfolk, K., Rosenholm, J.B.: Temperature-dependence of electrical and dielectric properties of papers for electrophotography. J. Appl. Phys. 107, 114904 (2010).https://doi.org/10.1063/1.3386466